Characterization and modeling of large collapsible tubular mast booms

Olive R. Stohlman[1]
NASA Langley Research Center, Hampton, VA, 23681, USA

Martin E. Zander[2]
Institute of Composite Structures and Adaptive Systems, DLR German Aerospace Center, Braunschweig, 38108, Germany

Juan M. Fernandez[3]
NASA Langley Research Center, Hampton, VA, 23681, USA

This paper documents the analysis of high-strain composite booms in the joint NASA-German Aerospace Center (DLR) Deployable Composite Booms (DCB) project. The collapsible tubular mast (CTM) booms were manufactured at NASA Langley Research Center, where constituent material coupons were also characterized, and shipped to DLR in Germany for testing of beam properties and the strength of the DLR flight-like root deployer design. With this data, a finite element model of the booms was built, calibrated to one set of experimental measurements, and used to produce a simplified beam model for further engineering studies. The process of building this beam model and the treatment of gaps in experimental characterization are presented.

I. Introduction

Most high-technology-readiness deployable space structures are designed for medium- to-large-sized satellite and spacecraft applications. The lack of reliable deployable structural systems for low cost, small volume, rideshare-class spacecraft, such as CubeSats, currently limits the potential of small satellite platforms for use in low-cost science and exploration missions. Deep space missions, where relatively large deployed structures are required for power, communications, and in some instances propulsion, are particularly limited. NASA is currently investing in the development of a new class of advanced deployable thin-shell composite booms to support future deep space small satellite missions [1]. These boom concepts are being designed to meet the unique requirements of small satellites. These requirements include: packageable into very small volumes, testable on the ground in an Earth-gravity environment, inexpensive to manufacture, scalable for use as elements of hierarchical structures (e.g. trusses), capable of being stored for long periods without significant distortions in deployed shape, high deployment reliability, controlled deployment behavior, and predictable deployed dynamics.

The Deployable Composite Booms (DCB) project is an ongoing collaboration between NASA and the German Aerospace Center (DLR) to improve the state-of-the-art in rollable high-strain composite booms and associated deployment mechanisms. It has the near-term goal of perfecting booms for large CubeSat-class solar sails and other small satellite applications requiring 5-to-20-meter booms [2], and the medium-term goal of producing much longer booms as well as boom trusses. The project has produced 16.5 m long rollable high-strain composite collapsible tubular mast (CTM) booms out of experimentally characterized materials, and tested the as-manufactured performance of these ultra-lightweight deployables in the lab, with and without a realistic root boundary condition [3]. The realistic root condition is based on a boom deployer mechanism concept with a supported transition zone sleeve, also developed

[1] Research Aerospace Engineer, Structural Dynamics Branch, AIAA member
[2] Research Aerospace Engineer, DLR Institute of Composite Structures and Adaptive Systems
[3] Research Aerospace Engineer, Structural Dynamics Branch, AIAA member

for the 27U CubeSat size as a part of the DCB project [4]. Figures 1 (a) and (b) show a 16.55 m boom deployed and partially rolled on a 180 mm diameter cylindrical spool, as well as the dedicated large equipment built to fabricate the booms. This equipment includes low coefficient of thermal expansion carbon molds, tunnel composite curing convection oven, rolling cart and other hardware for rotating, lifting, coupling and separating the molds.

This paper will focus on the correlation of testing and analysis in the DCB project. 7 m CTM booms with a smaller cross-section will be flight validated as part of the Advanced Composites Solar Sail System (ACS3) flight demonstration mission in Low Earth Orbit expected to launch circa the end of 2021 [5]. The larger 16.55 m CTM booms were sized to the application of a large Cubesat-class solar sail, of 500 m^2 in a 27U CubeSat small satellite. At this stage of development, it is important to establish an approximate range of realistic boom structural performance. Armed with this realistic understanding of cutting-edge boom performance, we can greatly increase confidence in solar sail performance. Boom strength impacts tensioning levels in the sail, and perhaps more significantly, boom variability impacts our a priori knowledge of the sail shape, an important input to attitude and thrust control systems, and a fundamental solar sail design requirement [6].

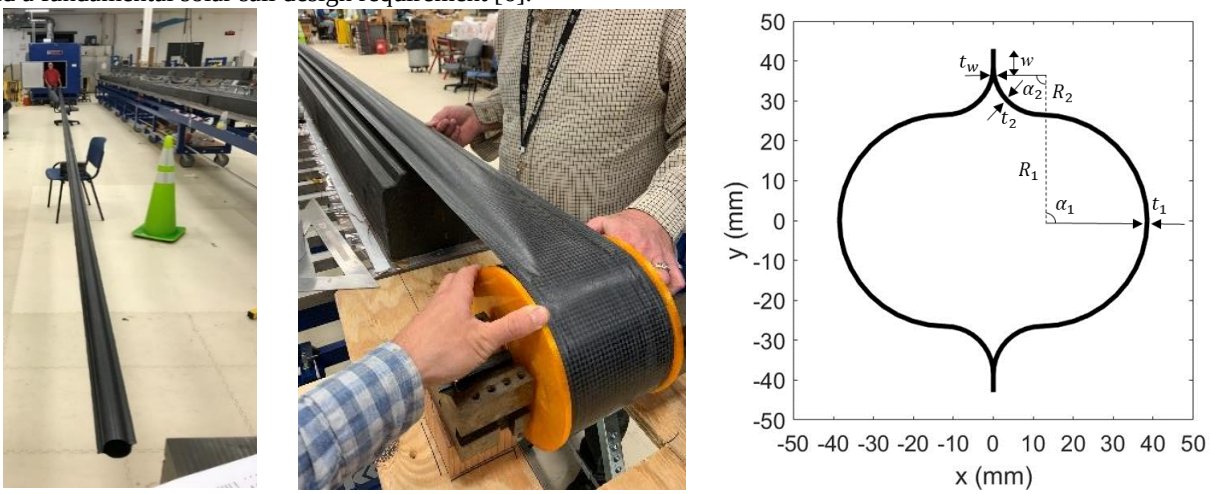

(a) (b) (c)

Figure 1: 16.55 m CTM boom deployed (a), partially rolled on a spool (b), and cross-sectional geometric parameters (c).

The remainder of the paper is organized as follows. Section II describes the nominal boom design and the material characterization that was used for the model. In Section III, experimental measurements of static boom loading and displacement for 9- and 13-meter booms are presented. The modeling, in Section IV, is broken down into the modeling of an ideal root condition (Section IV.A), used for calibration of beam model; the real root condition (Section IV.B), which was not fully captured by modeling; and the derivation of a beam-element model in Section IV.C from the experiments and tests. Conclusions and forward work are described in Section V.

II. Boom design and characterization

The closed cross-section geometry of the CTM boom, seen in Figure 1(c), was selected for its superior bending and torsional stiffness and strength over competing open or partially-closed cross-section designs [1]. Additionally, a higher dimensional accuracy was achieved during manufacturing. This translates to a boom design that is more scalable and has a more reliable deployment process.

The specific cross-sectional geometry was selected to maximize the area moment of inertia about the weakest axis of the boom and the torsional constant, which translates to an adequate compromise of bending stiffness about both principal axes and improved torsional stiffness. The CTM geometry consists of two thin-shell omega-shaped halves formed by three tangent circular arc segments that are bonded at flat regions called the web.

Segment 1 is associated with the radius of curvature R_1, subtended angle α_1 and thickness t_1, and segment 2 with R_2, α_2, and t_2 as shown in Figure 1(c). To prevent kinks between segments 1 and 2, α_1 must equal α_2, which means only a single subtended angle and either R_1 or R_2 could be specified during the optimization process. With h the flattened height of each shell, w the width of the web, and t_w the web thickness, Equations (1) and (2) show the relationship between R_1, α_1, R_2, and α_2,. Tangent continuity between shell segments is a design goal; modeling considers the possibility that the as-built shape may have small deviations from tangency.

$$h = 2\,(w + L_1 + L_2) \tag{1}$$

$$L_{1,2} = R_{1,2}\alpha_{1,2} \tag{2}$$

Table 1 shows the nominal geometrical parameters of the optimized pristine CTM boom. These define the geometry of the boom molds. Several factors caused differences between as-manufactured booms and the intended optimal shape. The most critical of these were the thinness of the laminates involved and the relatively large radii involved, which did not provide much structural depth, or out-of-plane stiffness, to the parts. Using asymmetric laminates for some of the shell segments also induced thermo-elastic deformations during the boom curing process at high temperatures. These thermo-elastic deformations resulted in permanent deformations and residual stresses once the parts returned to room temperature. The coefficient of thermal expansion (CTE) mismatch between the part and the mold also produced a similar effect on the final shape of the boom structure. Both effects were exacerbated by the small wall thickness of the shells. Cure induced deformations of ultra-thin composite shell laminates are notoriously prominent and challenging to analyze [7] [8]. In order to find the as-built geometry of the boom, its cross-sectional width and height were measured at different positions on the boom, photographs of the boom ends were used for arc fitting, and laser scans of boom segments were taken. These measurements also provided a jumping-off point for understanding part variability.

Table 1: Nominal geometrical parameters of optimized pristine CTM boom.

h (mm)	R_1 (mm)	R_2 (mm)	α_1 (°)	α_2 (°)	t_1 (mm)	t_2 (mm)	t_w (mm)	w (mm)
130.00	26.50	12.00	90	90	0.18	0.12	0.34	4.50

Table 2 shows the material properties of the thin-ply composites and adhesive used in the different shell laminates of the boom. The theoretical Young's moduli E_1 and E_2, Poisson's ratio ν_{12}, shear modulus G_{12}, and thickness t properties of the spread-tow unidirectional (UD) and plain weave (PW) carbon fiber reinforced plastic (CFRP) materials listed were determined by micromechanics models and classical lamination theory (CLT) using the AutoDesk composites modeling software Helius Composites 2017. Fiber and matrix stiffness values from the manufacturer's datasheets, a nominal 60% fiber volume fraction (FVF) as specified in the prepreg process, and the nominal fiber areal weights of the purchased fabric were also used, and gave the lamina areal weights (AW) listed in Table 2.

Recent tensile and in-plane shear tests carried out at NASA on coupons cut from flat plates that were cured under the low pressures (<1 atm) of an out-of-autoclave process, just like the booms, and tested following the ASTM D3039M-14 and D3518M-13 standards have shown that the axial, transverse, and shear moduli are lower than the values derived from CLT and nominal material properties. For example, measured Young's moduli were 17.2% lower for the UD ply and 5.5% lower for the PW lamina. Some of this discrepancy can be attributed to the much lower measured fiber volume fractions of 52% and 56%, respectively, and to variable thickness of the thin-ply material. It is to note that the FVF of the composite plies in a thin-walled boom will be different than the FVF in the much thicker material coupons.

Table 2: Theoretical (t) and average empirical (e) material properties for the boom's thin-ply laminae and adhesive.

Label	Material Form	Fiber/Resin	$E_{1,t}$ (GPa)	$E_{1,e}$ (GPa)	$E_{2,t}$ (GPa)	$E_{2,e}$ (GPa)	$\nu_{12,t}$	$\nu_{12,e}$	$G_{12,t}$ (GPa)	$G_{12,e}$ (GPa)	t_t (μm)	t_e min/max (μm)	AW (g/m^2)
$_C$	Unidirectional	MR60H/PMT-F7	174.4	144.1	8.4	5.2	0.259	0.335	6.4	2.8	40.0	40.0/42.0	63.4
PW_C	Plain Weave	M30S/PMT-F7	94.2	89.0	94.2	89.0	0.026	0.035	3.9	4.2	60.0	58.2/62.5	89.7
$_A$	Adhesive Film	Hysol EA9696	2.1	-	2.1	-	0.300	-	0.6	-	100.0	85.0/100.0	146.0

Table 3 shows the laminate of each shell segment of the boom (segment 1, segment 2 and web) according to those reflected in Figure 1(c). CLT in Helius Composites was used to determine the laminate mechanical properties assuming a combination of the theoretical and empirical properties from Table 2. The so-called thin (TN) laminates assumed plies built from new micromechanical models with the average empirical mechanical properties and the lower bound (minimum) of the experimental thickness values measured on the flat plates. This model was built as a lower stiffness limit for the boom laminate. The so-called thick (TK) laminates assumed plies with the theoretical stiffness properties and the upper bound (maximum) of the experimental thicknesses measured on the flat plates. This model

was built as an upper stiffness limit for the boom laminate. Coupons with the boom laminates from segment 1 and 2 cut from flat plates were tested following the ASTM D3039M-14 standard. For segment 1, the measured average E_1 was 46.4 GPa and the E_2 was 21.58 GPa, which aligns more with the calculated thin laminate properties listed below. For segment 2, the measured average E_1 was 68.3 GPa and the E_2 was 13.0 GPa. For both laminates, the empirical moduli align better with the calculated ones with the thin laminate properties. This means that laminate models built from experimentally-derived ply properties and assuming thinner plies are likely to represent better the physical test articles than those generated from theoretically-derived properties and assuming thicker plies. Further measurements taken from boom sections will similarly help refine the material models used to analyze the long boom articles tested.

Table 3: Laminate properties used in the different sections of the boom finite element models.

Segment	Laminate	$E_{1,TN}$ (GPa)	$E_{1,TK}$ (GPa)	$E_{2,TN}$ (GPa)	$E_{2,TK}$ (GPa)	$\nu_{12,TN}$	$\nu_{12,TK}$	$G_{12,TN}$ (GPa)	$G_{12,TK}$ (GPa)	t_{TN} (µm)	t_{TK} (µm)
1	$[45PW_C/0_C/45PW_C]$	47.9	55.5	24.8	27.5	0.824	0.819	32.7	36.0	156.4	167.0
2	$[45PW_C/0_C]$	68.5	79.9	14.4	15.7	0.822	0.819	14.8	19.7	98.2	104.5
web	$[45PW_C/0_C/0_A/0_C/45PW_C]$	48.4	54.7	17.6	18.8	0.781	0.776	18.8	20.5	281.4	309.0

III. Characterization of bending properties

Mechanical metrics of the booms, such as stiffness and buckling load, were acquired using the boom test stand in the DLR Space Structures Lab at the Technical University of Braunschweig, in Braunschweig, Germany [9] [10] [11]. This facility enables mechanical testing of long booms in a vertical orientation. No additional gravity compensation is used, as the booms are self-stabilizing and under their own weight, though gravity is included in finite element simulations of the tests. Booms of 9.18 m and 12.76 m length were mounted in boom root fixtures and interfaces that represent ideal and realistic boundary conditions. The changes in boom stiffness with these differing boundary conditions were used to distinguish the effect of the deployer root condition in later simulations.

Throughout this paper, "in-plane" and "out-of-plane" bending are used to indicate bending in and out of the plane of a solar sail, as shown in Figure 2. In Figure 1(c), "in-plane" bending is about the cross-section's y-axis, and "out-of-plane" bending is about its x-axis. In the experimental laboratory frame, defined in Figure 3, all bending is about the y-axis, and the boom was rotated to test different bending directions.

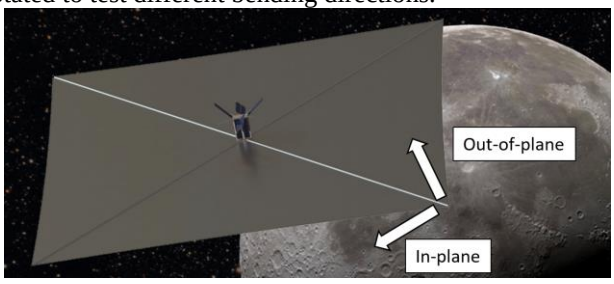

Figure 2: The in-plane and out-of-plane directions are defined by the plane of a solar sail.

A. Principle & Methodology

The loads were applied by a string in a test rack (see Figure 3); the load angle of 10 degrees ("in-plane") was selected as a realistic solar sail boom loading angle and a 90-degree loading configuration was used for destructive testing. While deflecting the boom tip under an angle of attack α, string tensile forces are measured and boom tip deflections and rotations in all 6 DOF are tracked using a photogrammetry system. This gives not only a measurement of the ultimate loads but also a complete picture of the load-displacement curve of the booms.

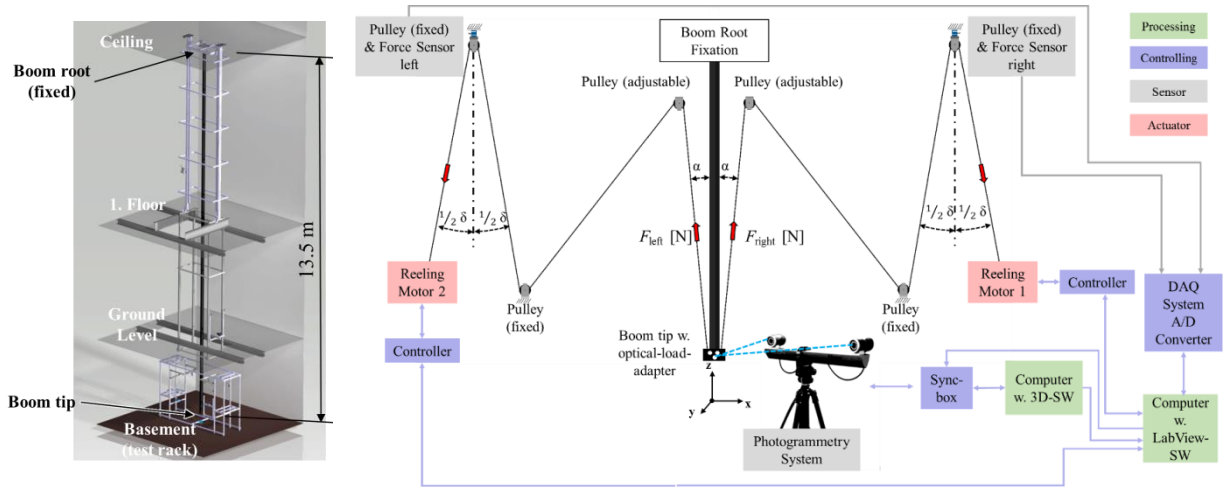

(a) Laboratory installation of the boom test stand

(b) Functional scheme of the boom test stand

Figure 3. Mechanical boom test stand (force sensors are calibrated with static weights).

B. Test Stand & Setup

The test facility spans multiple levels of a single lab as depicted in Figure 3(a); the lowest level, where loads are applied and boom deflections are measured, is shown in Figure 4.

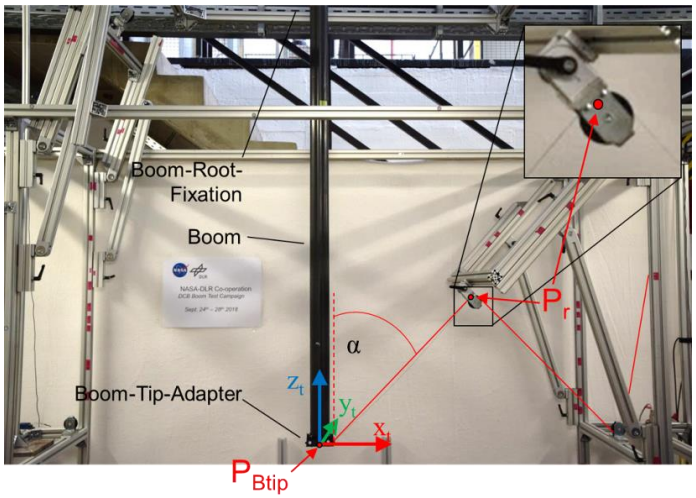

Figure 4. General test setup and test coordinate system.

A few stories above the boom tip, at the root fixation (see Figure 3(a)), three different root boundary conditions were considered. The first, the "ideal" root boundary, is shown in Figure 5(a). This ideal boundary was used for characterization of the deployed boom as a beam. Two "real" boundary conditions were also measured, both based on the design of the DCB project's proposed boom deployer. Figure 5(b) shows the real "clamped" root condition that occurs at the end of deployment, the long-term condition for a solar sail. In this condition, the end of the boom is fixed to the boom hub with a flattened root, and passes through a support sleeve that is fixed to the hub. Figure 5(c) shows the real "partially deployed" root condition, which is the condition of the boom shortly before the end of deployment. In this condition, the flattened part of the boom is wrapped ¼ of the way around the hub, and the sleeve is not locked into the hub, but can rotate about its hinge axis. At the same time a restoring force is applied to the sleeve by the thin steel tape that serves as the deployment mechanism. This might be considered the "worst case" boom deployment condition, where the boom is as long as possible, but the root is not yet locked.

The “ideal” tip condition fully clamped the boom tip in an optical load adapter (Figure 6(a)), which enabled accurate 6-DOF tracking of the boom tip displacement and rotation. A flight-like boom tip (Figure 6(b)), which provided fewer optical targets, was used for the “real” root boundary conditions.

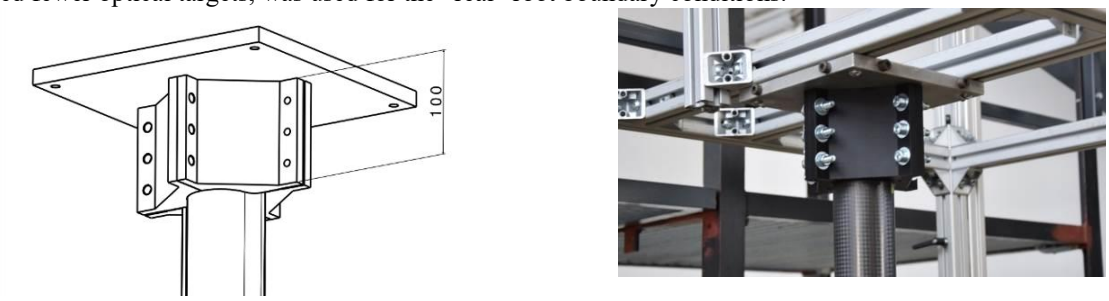

(a) Ideal clamped root boundary condition. The root condition also included an internal plug.

(b) Real clamped root boundary condition (at end of deployment).

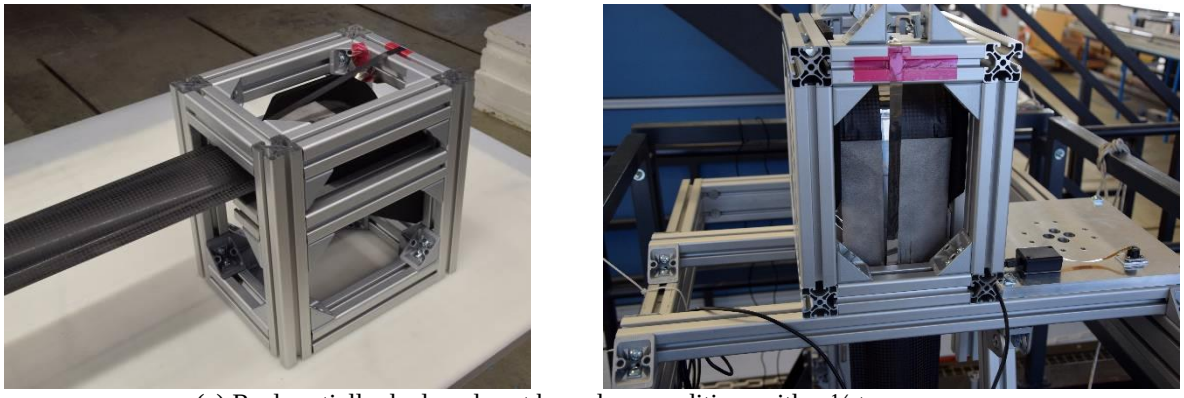

(c) Real partially deployed root boundary condition, with a ¼ turn-wrap.

Figure 5. Boom root boundary conditions for testing.

(a) Optical load adapter on boom tip for the ideal test configuration

(b) Boom-tip-sail interface on boom tip (real test configurations)

Figure 6. Adapter and interfaces for load introduction and photogrammetry measurements at the boom tip.

C. Test Results

The test results, shown in Figure 7 and Figure 8, are load-displacement curves for each configuration. These graphs show the tip displacement in the laboratory x-direction and the load in the loading string. The test configuration was unchanged between tests of the same boom. Non-destructive test results were used to determine bending stiffness, verify test repeatability, and calibrate the behavior of the finite element models. In order to characterize the boom´s ultimate mechanical capabilities, a destructive test, delivering the buckling load at bending failure, was performed by applying the load at 90 degrees to the boom. Results from this destructive test, which was preceded by non-destructive testing in the same configuration, are shown in Figure 9.

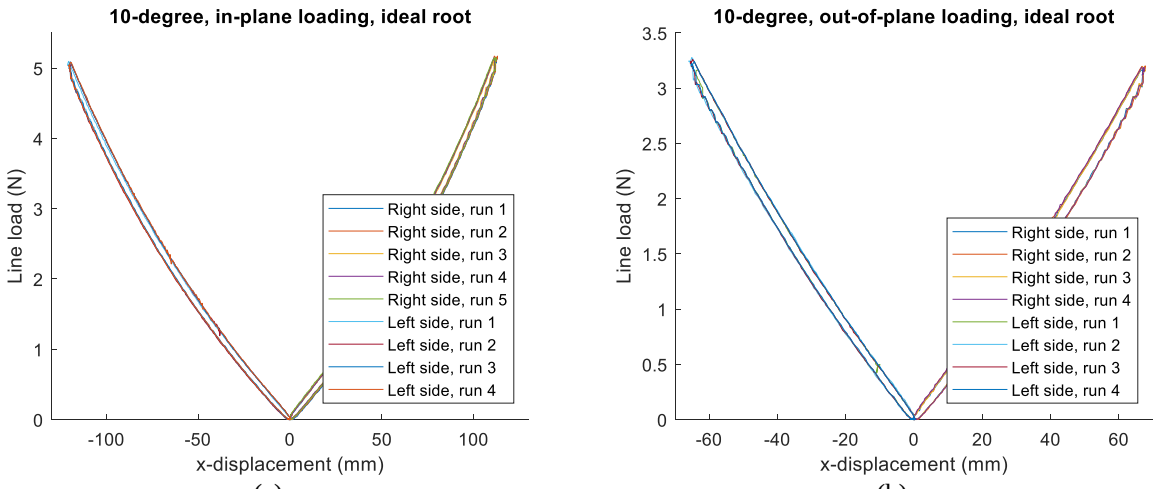

(a) (b)

Figure 7: Results from non-destructive mechanical bending tests at a 10° angle of attack for the ideal root condition for in-plane (a) and out-of-plane (b) directions.

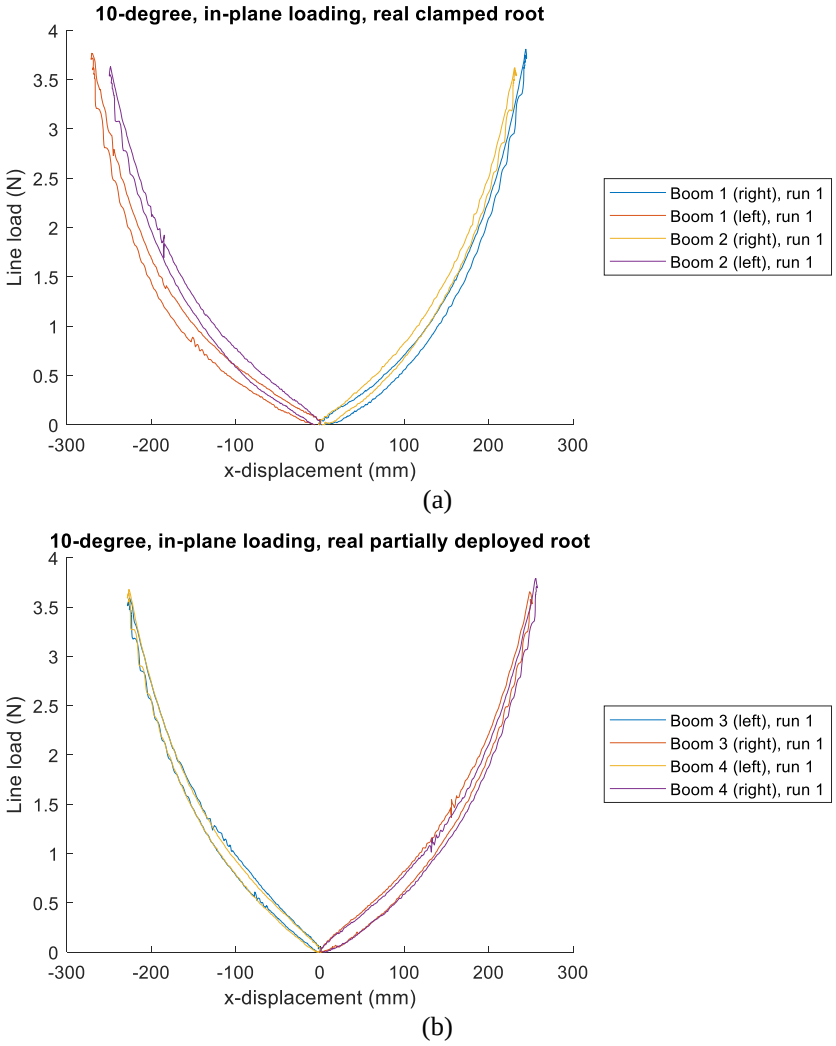

Figure 8: Results from non-destructive mechanical bending tests at a 10° angle of attack for the real clamped (a) and real partially deployed (b) root conditions. As in the ideal case, tests were repeated five times; only the first repetition is shown.

As expected, the boom, which was taller than it was wide, was stiffer in out-of-plane bending than in-plane bending. The boom was also softer when supported in the real root boundary condition, which was expected because the cross-section is not fully developed when it exits the support sleeve. Interestingly, the differences between the real clamped case and the real partially-deployed case were no larger than boom-to-boom differences within the real clamped case. This indicates that the partially deployed root and the clamped root have similar structural performance, and that it may be acceptable to use the same model for the boom root both during and after deployment. The two conditions could diverge at very high loads, however, if the partially deployed boom were jammed or forced backwards into the deployer, causing boom blossoming [12].

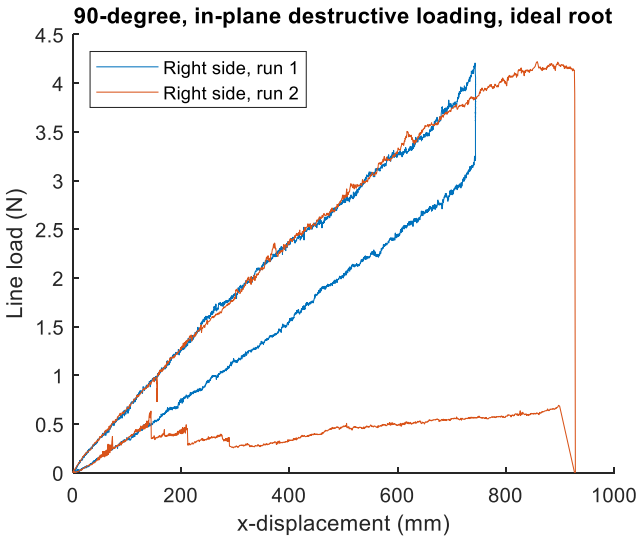

Figure 9. Destructive and non-destructive mechanical bending test results at 90° angle of attack for the ideal clamped configuration. The redirection point was moved between tests to allow for a larger range of motion.

Significant hysteresis was observed in the non-destructive 90-degree tests, with a large drop in load between loading and unloading that exceeded the drop at the same loads and at the same displacements in 10-degree testing. A clear explanation of this increased hysteresis has not been identified; the only change in the experimental apparatus was in pulley position.

IV. Modeling

Finite element analysis (FEA) was performed using Abaqus/Standard. There were two goals: to create a shell-element model that showed good agreement with the bending experiments, and to create a beam model that matched the bending experiments in the linear regime.

A. Ideal root shell model

The shell model was built with approximately 34,000 S4R elements for the 9.18 m boom tested in the ideal loading condition and 47,000 elements in the 12.76 m booms used for the real root conditions. The as-modeled boom cross-section, informed by material and cross-sectional measurements described in Section II, is shown in Figure 10.

A range of simulated boom cross-sections were compared with the experimental data. The width and height of the boom have a direct relationship with the in- and out-of-plane bending stiffnesses, and the kink angle between the two arcs of the cross-section has a less significant impact on stiffness. Many realistic combinations of material properties and cross-section produced good fits to the experimental data. The shell model has more parameters available for calibration than the experimental data on the ideal boom root required. This left some margin for the model to also be calibrated against the destructive tests and the real root condition; however, as discussed in Section IV.B, fitting these results proved difficult.

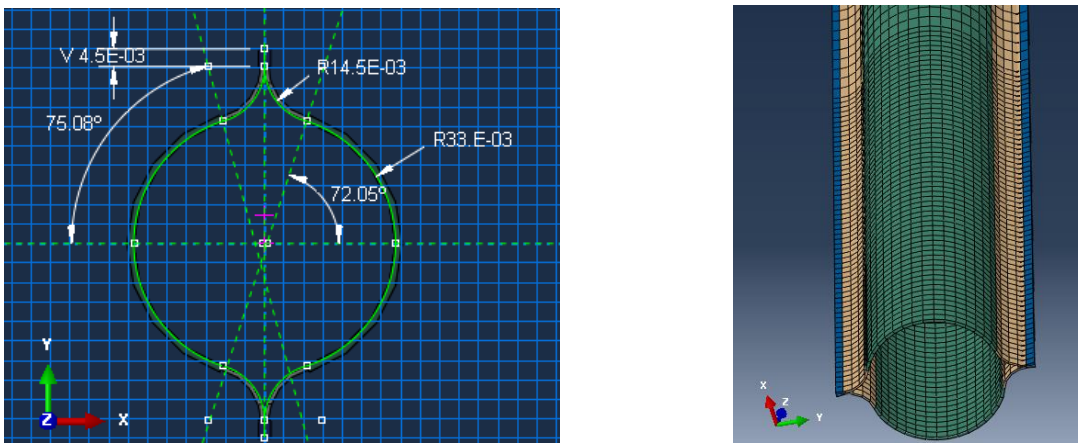

(a) (b)

Figure 10: Modeled boom dimensions (a) and section thickness geometry, visualized at 10x thickness (b). Modeled dimensions differed from the nominal dimensions of the boom (Table 1), and were based on height and width measurements of the boom cross-section and earlier fitting data. A tangency condition was not enforced between the two arcs.

1. 10-degree loading case simulation results

The in-plane, 10-degree, "ideal" root case had a good match between simulation and experiment for the "thick" material model. The out-of-plane performance was matched well by the "thin" material model. The correct model lies between the two, and many possible combinations of materials and cross-sectional shapes showed an acceptable fit.

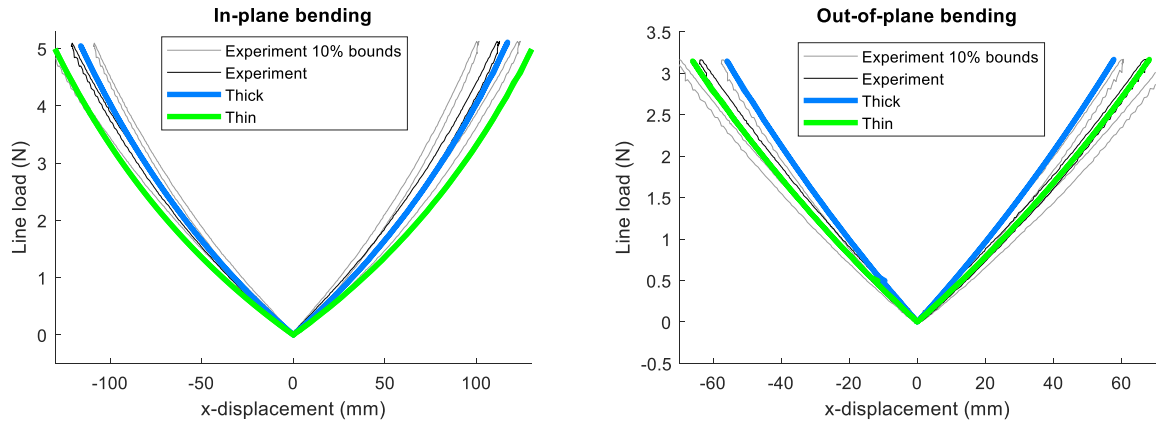

(a) (b)

Figure 11: In-plane (a) and out-of-plane (b) experiment and shell model simulation.

Further material testing is ongoing and will tighten the limits on the possible material properties. For the purposes of creating a beam model that reproduces the bending stiffness of the boom, a knockdown factor was applied to the axial stiffness of the material in the small shell segment defined by R_2 and α_2. Having this calibrated shell model made it possible to easily extract the linear bending and torsional stiffnesses of the boom in Section IV.C.

2. 90-degree destructive loading case simulation results

Using the shell model that was calibrated to the 10-degree in-plane loading case, the 90-degree destructive test was simulated. As shown in Figure 12, the simulated load-displacement curve fell between the experimental loading and unloading curves for this case, and the boom failed at the same ultimate displacement. These results appear, at first, to be a remarkably good match between experimental and simulated behavior. However, alternate models that also showed good agreement in bending stiffness did not agree well. The destructive loading case is sensitive to

parameters that are not currently well-characterized, and will be revisited as the precision of the material and geometric model improves.

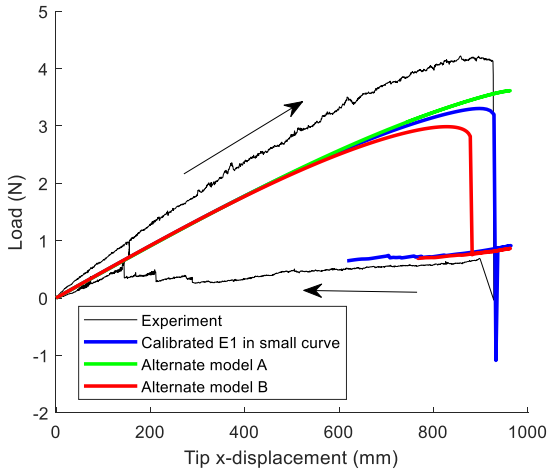

Figure 12: In-plane 90-degree-loading destructive testing experiment and simulations.

B. Real root shell model

Numerically modeling flattening and rolling of the root of a high-strain composite rollable boom formed by two bonded thin shells is often a time-consuming computation, and several different approaches have been used recently [13] [14] [15] [16] [17]. It is also often a trial-and-error process.

In the real root condition, the boom emerges from the deployer through a rigid plastic sleeve. The shape of this sleeve was based on scans of the natural transition shape of the boom from a fully flattened end. The sleeve was modeled as a rigid body in Abaqus, using a frictionless contact condition with the boom.

Root compression was simulated in a stabilized STATIC step, shown in Figures 12(a)-(c). It was accomplished by applying displacement boundary conditions to the boom root to maintain its position in space and moving the sleeve in from the +X side and the hub with a second copy of the sleeve from the –X side. The two sleeves are constrained to equal rotations using an ALIGN connector element. This method, where the two contact conditions move in to sandwich the boom from the sides, was reached after failed simulations where the boom root was flattened and drawn through a stationary support sleeve.

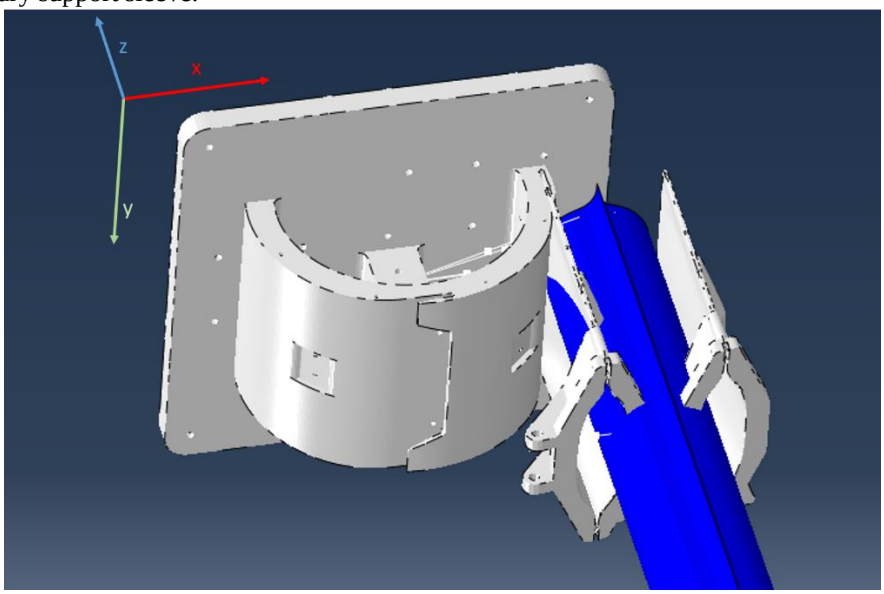

(a)

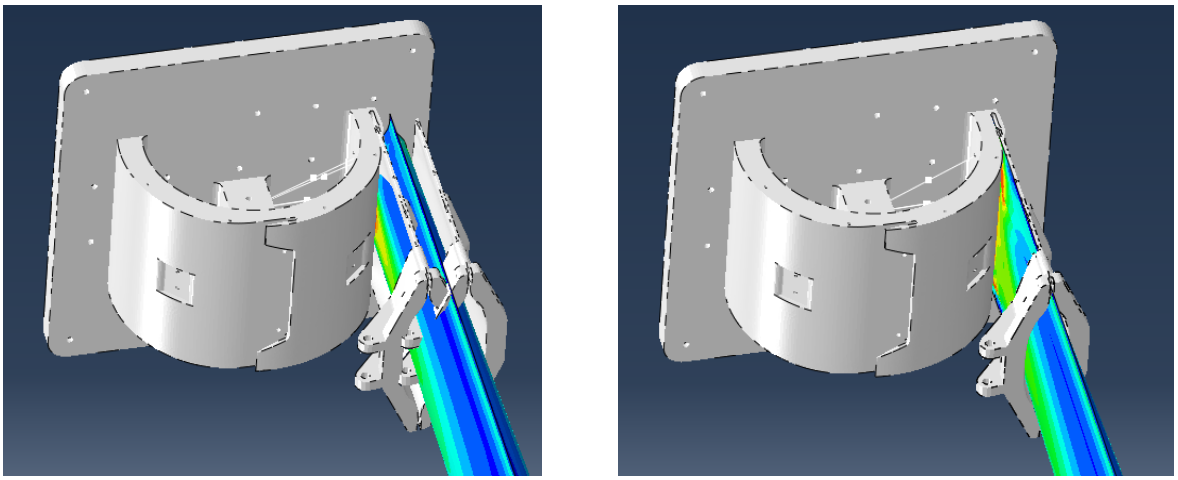

(b) (c)

Figure 13: The boom root compression process. The hub and two copies of the sleeve, one for each side of the boom, are initially not in contact with the boom (a), though non-contact surfaces intersect. In the compression step, they are moved in from the sides and come into contact with the boom (b) until the two copies of the sleeve are merged (c) and no intersections remain.

1. Real clamped loading case simulation results

Simulated loading of the boom in the real root condition gave a poor fit to the experimental data. The discrepancy is shown in Figure 14. The simulated results show a large region of low stiffness around the boom's undeformed equilibrium position. Outside of this region, there is some resemblance between experimental and simulated stiffness at the same load.

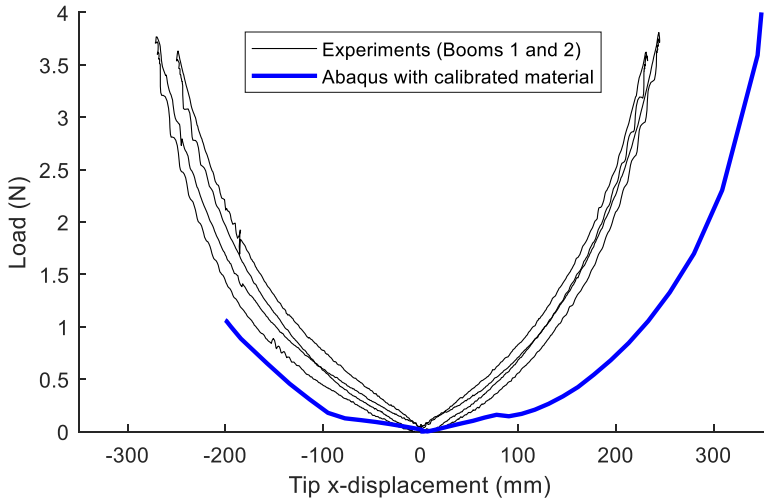

Figure 14: Results for the simulation of the real clamped root condition, showing an apparent deadband at low displacements.

During testing, the boom was observed to fill the sleeve at its center section, coming close to contacting it around the lip. In the simulation, there is a significant gap between the boom and the sleeve, as seen in Figure 15. This indicates that either the cross-sectional shape or the material model of the boom is not fully captured. Minor changes to the material model, such as a 20% increase in the boom's hoop-direction stiffness (E2), did not significantly change the simulated fit of the boom within the sleeve. Minor changes to the cross-sectional shape also did not produce an improvement in fit.

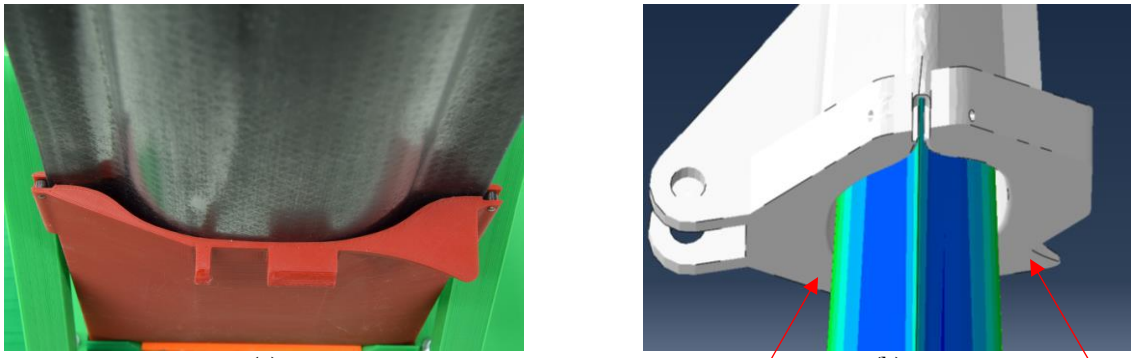

(a) (b)

Figure 15: A close view of the experimental (a) and simulated (b) booms in the support sleeve, showing that the boom touches the lip of the real support sleeve, but does not make contact at this point in simulation.

2. Real partially-wrapped configuration

For the real partially-wrapped configuration, an additional step was added to wrap the boom ¼ turn around the hub. So that the hub and boom would rotate together, a CARTESIAN connector element was added between the reference node for the hub and the boom nodes that represented the boom's root bolt holes. After the boom root was compressed, a velocity boundary condition was applied in the (initial) Y and Z directions of these connector elements. This constrained the end of the boom to rotate with the hub. The support sleeve, rather than being fully locked, was permitted to rotate about its hinge, with a continuous moment of 1 N-m compressing it against the boom and hub. In this configuration, a 90-degree rotation of the hub was performed in a stabilized STATIC analysis step. Stabilization was then removed for loading steps. This compression and rolling procedure is presented here as a point of interest, but results were not pursued because of the significant discrepancy in sleeve fit seen in Figure 15.

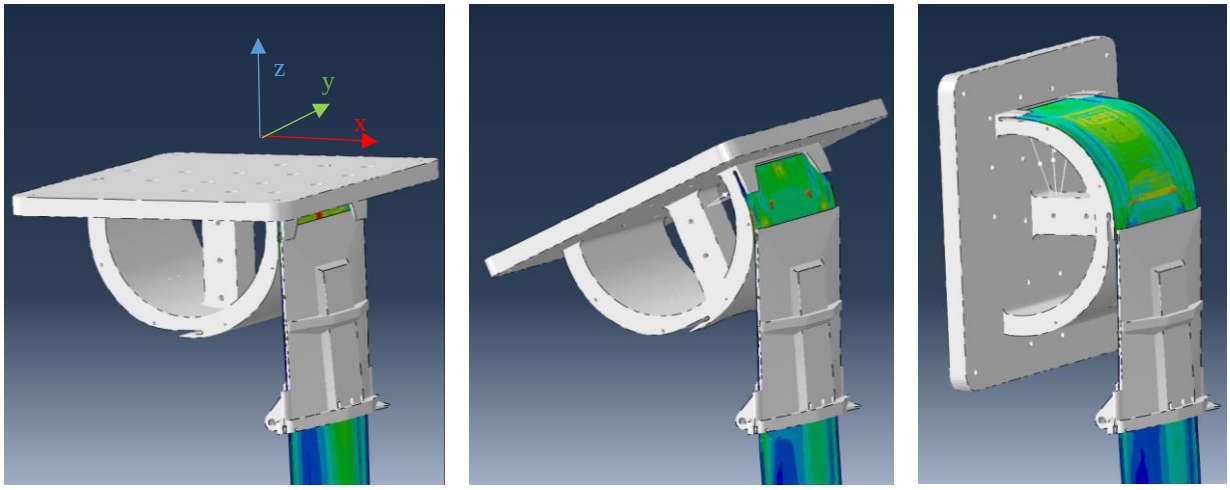

Figure 16: Hub rotation for the partially-wrapped configuration.

C. Derivation of the beam model

The bending stiffness of the booms can be directly derived from the ideal experiments, but the torsional stiffness was not measured, and the geometry of the test setup includes some geometric irregularities. It is simple to run idealized bending and torsion simulations on the shell model and convert this into a linear beam, applying pure moments to the boom tip and measuring displacements in the linear regime.

An Abaqus BEAM GENERAL SECTION can be generated from this data with some knowledge and assumptions about the materials. The beam stiffnesses $EI_{xx}, EI_{yy},$ and JG for out-of-plane, in-plane, and torsional behavior can be determined by applying a pure moment to the tip of a long simulated boom, and the Young's modulus E and shear modulus G are assumed to be areal averages of the composite material properties. A beam derived in this manner from

the shell model was subjected to the experimental loading conditions, including identical geometric offsets, and the results are shown in Figure 17. Up to the loading levels considered in this study, this is a good model that captures the linear behavior of the boom.

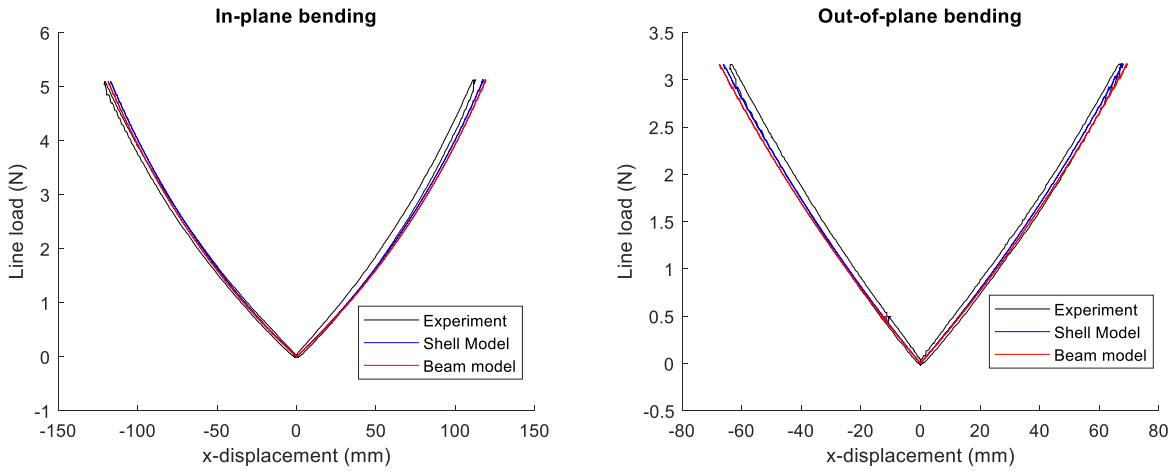

Figure 17: Comparison of experiment, shell model, and beam model.

The beam model can be combined with a nonlinear spring hinge at the root to capture the weakening effect of the real root condition. Such a model assumes that the effect of the partially flattened root is localized, so that the boom effectively rotates about a single point, as in Figure 18. The validity of this assumption is expected to improve with the length of the boom, and could be evaluated by tests on booms of different lengths, or by a shell model that correctly captures the real root behavior.

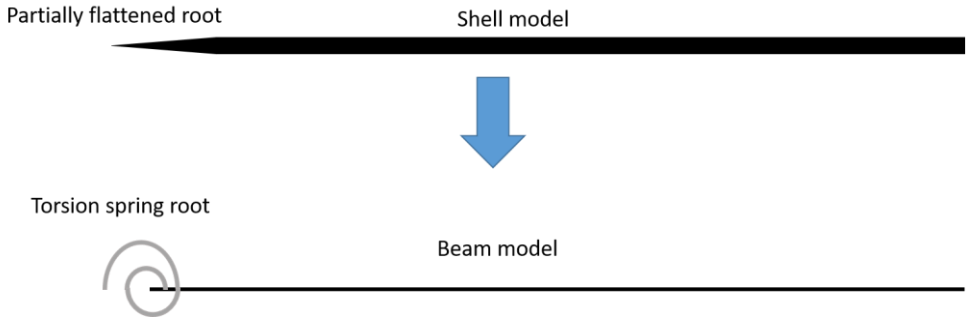

Figure 18: The shell model of the boom is reduced to a linearized beam model with a torsion spring at the root.

To calibrate this equivalent hinge, we find the difference between the angular displacement of the boom tip in the real, clamped experimental condition and the expected angular displacement of the boom tip in a statically equivalent ideal condition. The geometry of this method is outlined in Figure 19.

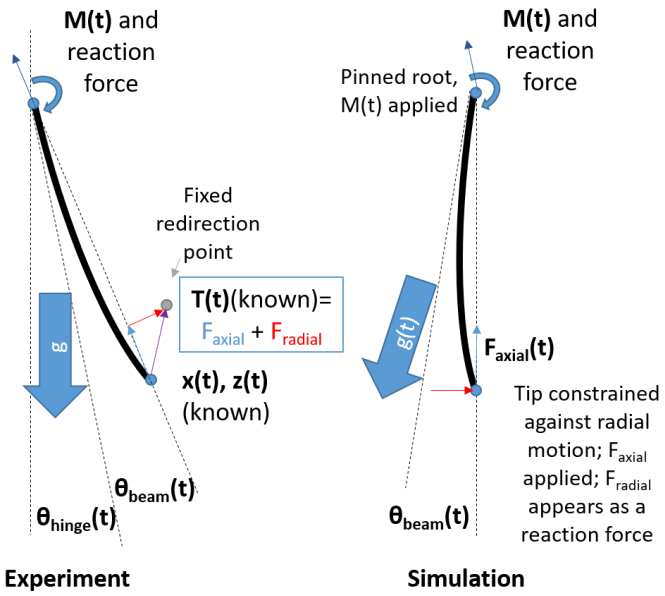

Figure 19: Derivation of the equivalent root hinge from simulation and experiment. A simulation can be used to separate the experimental tip displacement that is due to beam bending from the displacement that is due to root weakness.

Because the angle and magnitude of the load of the boom tip are known, the root moment due to the applied load is known. The root moment due to gravity, however, depends upon the deformed boom shape; the simulation was first run with an assumption that the boom remained straight, and the root moment due to gravity was recalculated based on the simulated boom shape. The root moment due to gravity converged after a single iteration of this process.

The output of this simulation is the value $\theta_{beam}(t)$, which is then subtracted from the observed tip displacement of the boom. This calculation is shown for all tested booms in Figure 20. A smoothed, averaged equivalent hinge model is shown in Figure 21.

At this length, both beam bending and the weakened real root are significant contributors to the overall behavior of the boom. It is possible that the boom-to-boom variability in the real root configuration is largely due to differences in boom stiffness or shape; Boom B1L and B2L were tested in the real clamped condition, and B3L and B4L were tested in the real partially-deployed configuration.

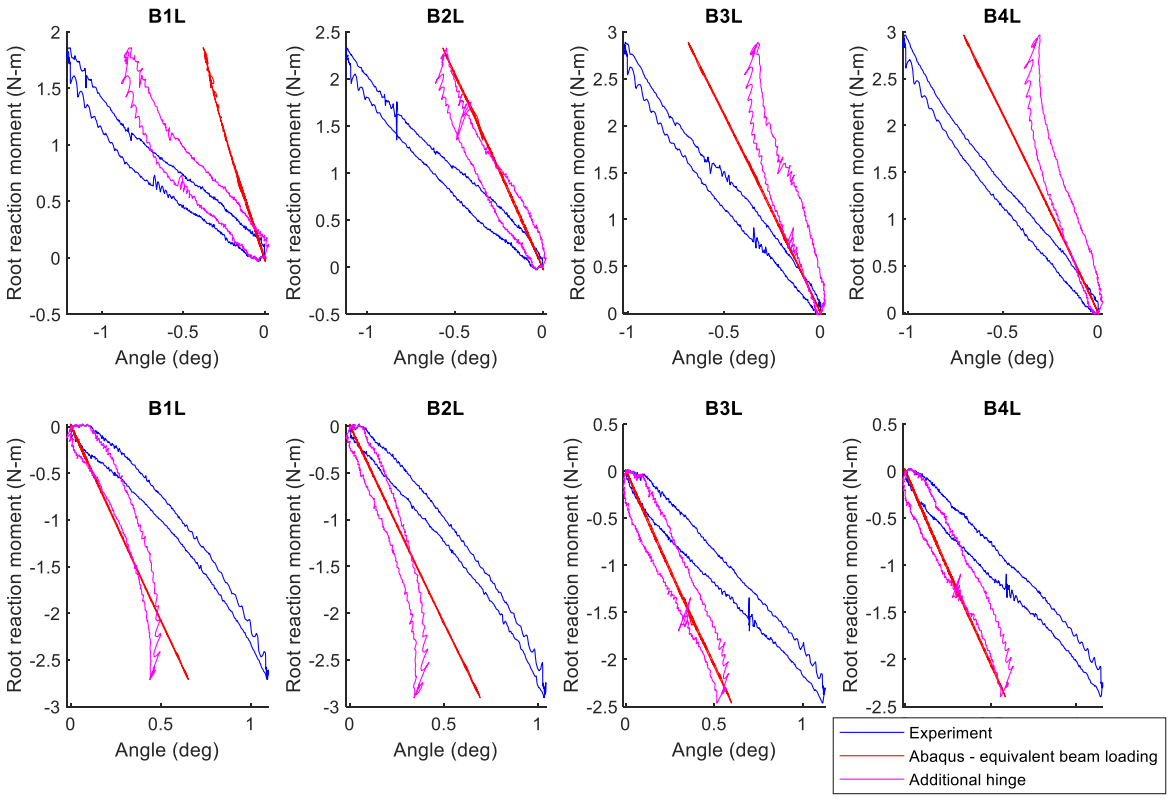

Figure 20: Angular displacement of the boom tip due to beam bending and real root condition effects.

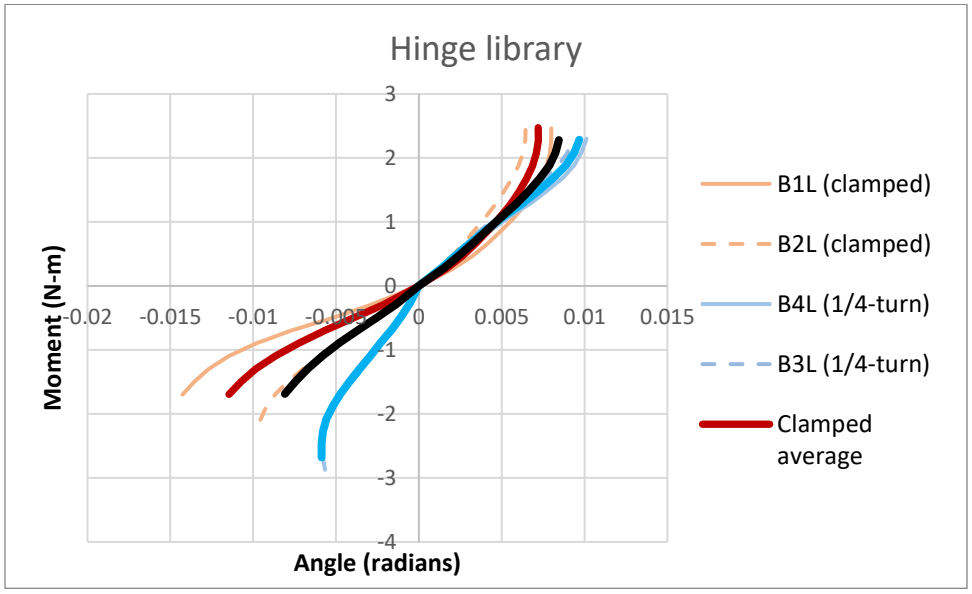

Figure 21: All equivalent hinges and a smoothed average hinge. From the small sample size, it is not obvious whether the real, clamped condition is significantly different from the real, ¼-turn condition.

The root condition also affects the out-of-plane stiffness and torsional stiffness of the boom. These conditions were simulated in Abaqus, using the real, clamped shell model. In simulation, the out-of-plane displacement of the boom tip was only 2% greater for a boom in the real sleeve than a boom with an ideal boundary condition; because this is smaller than the boom-to-boom variation in stiffness, there is no benefit to modeling a reduction in out-of-plane boom root stiffness at this boom length. A linearized torsional stiffness was derived from the shell model of the real, clamped

boom, with a stiffness of 12.5 N·m/rad. On a simulated 12.8-meter boom, torsional behavior was dominated by the effect of the real root condition, rather than by twisting of the boom.

With a linear 3-D beam model and a 3-DOF root hinge spring to simulate the weakening due to the root condition, this characterization of the booms becomes a useful tool in large structures design. A number of interesting questions remain, particularly with respect to the poor fit of the model to the "real" root condition experiments, and the model will certainly improve with the quality of the material characterization. Nonetheless, the experimental data and the linearized beam model based on this data are completely sufficient as inputs to mission development. With a realistic beam and root model, other structural designs concerns can be rapidly iterated and manufacturing tolerances, like boom straightness, can be investigated for their impact on mission performance [6].

V. Conclusions and forward work

This paper has presented a step-by-step example of how complex, and in some places incomplete, experimental data can inform a simplified beam model of a high-strain composite boom. It describes the derivation of the material model and supplemental information about the experimental bending measurements that were undertaken, and follows these with the simulation steps that were taken to produce a practical elastic beam-and-hinge model that will allow structural analysts to rapidly iterate solar sail designs with these booms.

Ongoing work is focused in two areas: improving the material characterization with micrographs of shell segments from the as-built booms, and scanning the surfaces of as-built booms and partially-flattened booms, in an effort to identify the reason for the difference in boom root shape shown in Figure 15. Improved precision in the material model and the boom shape will reduce the number of fit parameters in the shell model of the boom, and lead to a model of the boom that is not only calibrated, but validated.

Acknowledgments

The authors would like to acknowledge the work of the Deployable Composite Booms (DCB) project team and the generous consultation of Jay Warren and Matthew Chamberlain.

References

[1] J. M. Fernandez, "Advanced deployable shell-based composite booms for small satellite applications including solar sails," in *4th International Symposium of Solar Sailing*, Kyoto, 2017.

[2] NASA Space Technology Mission Directorate, "Deployable Composite Booms (DCB)," 27 August 2020. [Online]. Available: https://www.nasa.gov/directorates/spacetech/game_changing_development/projects/dcb/. [Accessed 23 November 2020].

[3] J. M. Fernandez, S. A. Krizan and E. R. Dyke, "Thin-shell composite booms for solar sails: Design, manufacturings, and qualification," in *5th International Symposium on Solar Sails*, Aachen, Germany, 2019.

[4] M. Richter, M. Straubel, J. M. Fernandez, O. R. Stohlman and W. K. Wilkie, "Compact deployment control mechanism for the deployable backbone structure of a 500-m2-class solar sail," in *5th International Symposium of Solar Sailing*, Aachen, Germany, 2019.

[5] W. K. Wilkie, J. M. Fernandez, S. Horner, P. L. Brown, P. Banicevic, T. Denkins, O. R. Stohlman, G. Rose, J. Warren, N. Schneider, G. Dean, J. H. Kang, M. K. Chamberlain, M. Straubel and J. Heiligers, "An overview of NASA's Advanced Composite Solar Sail System (ACS3) low-Earth orbit technology demonstration project," in *5th International Symposium on solar sailing*, Aachen, Germany, 2019.

[6] O. R. Stohlman, M. K. Chamberlain, M. E. Zander and W. K. Wilkie, "Structural modeling of a composite-boom-deployed solar sail with realistic part variability," in *5th International Symposium on Solar Sailing*, Aachen, Germany, 2019.

[7] J. M. Fernandez and A. J. Lee, "Bistability in collapsible tubular mast booms," in *AIAA Scitech Forum*, San Diego, CA, 2019.

[8] F. Bosi, A. Schlothauer and S. Pellegrino, "Cure-induced deformations of ultra-thin composite laminates," in *AIAA Scitech forum*, Kissimmee, FL, 2018.

[9] M. E. Zander, M. Hillebrandt, M. Sinapius and C. Hühne, "Mechanical characterization of deployable thin shell CFRP booms for the Cubesat "De-Orbit Sail"," in *The 66th International Astronautical Congress*, Jerusalem, 2015.

[10] M. E. Zander, M. Sinapius and C. Hühne, "Preliminary experiments for an on-orbit detection system to monitor load and deflection states of thin shell CFRP booms for the solar sail demonstrator Gossamer-1," in *CNES/ESA/DLR ECSSMET*, Braunschweig, Germany, 2014.

[11] M. E. Zander, A. Wilken, M. Sinapius and C. Hühne, "Mechanical testing of deployable thin shell CFRP booms in ideal and realistic interfaces for the solar sail demonstrator Gossamer-1," in *European Conference of Spacecraft Structures, Materials & Environmental Testing*, Toulouse, France, 2016.

[12] S. Wang, M. Schenk, H. Guo and A. Viquerat, "Tip force and pressure distribution analysis of a deployable boom during blossoming," *International Journal of Solids and Structures,* pp. 101-151, 2020.

[13] Y. Hu, Chen, W. Chen, J. Gao, J. Hu, G. Fang and F. Peng, "A study of flattening process of deployable composite thin-walled lenticular tubes under compression and tension," *Composite Structures,* vol. 168, pp. 164-177, 2017.

[14] C. Leclerc and S. Pellegrino, "Reducing Stress Concentration in the Transition Region of Coilable Ultra-Thin-Shell Booms," in *AIAA Scitech*, San Diego, CA, 2019.

[15] K. Cox and K. A. Medina, "Scalability of Triangular Rollable and Collapsible Booms," in *AIAA Scitech*, San Diego, CA, 2019.

[16] Y. Long, O. Rique Garaizar, J. M. Fernandez, A. C. Bergan and W. Yu, "Multiscale simulation of deployable composite structures," in *AIAA Scitech*, Virtual, 2020.

[17] H. Yang, L. Liu, H. Guo, F. Lu and Y. Liu, "Wrapping dynamic analysis and optimization of deployable composite triangular rollable and collapsible booms," *Structural and Multidisciplinary Optimization,* vol. 59, no. 4, pp. 1371-1383, 2019.